Advanced Engineering Materials

ADVANCED ENGINEERING MATERIALS
www.aem-journal.com

RESEARCH ARTICLE OPEN ACCESS

In Situ Micromechanical Study of Bimodal γ′–γ″ Precipitate Assemblies in Ni–Cr–Al–Nb Superalloy

Ujjval Bansal[1,2] | Tae-Hyeok Kang[3] | Pyuck-Pa Choi[3] | Subin Lee[1] | Christoph Kirchlechner[1]

[1]Institute for Applied Materials, Karlsruhe Institute of Technology, Karlsruhe, Germany | [2]Karlsruhe Nano Micro Facility (KNMFi), Karlsruhe Institute of Technology, Eggenstein-Leopoldshafen, Germany | [3]Department of Materials Science and Engineering, Korea Advanced Institute of Science and Technology (KAIST), Daejeon, Republic of Korea

Correspondence: Subin Lee (subin.lee@kit.edu)

Received: 29 November 2025 | **Revised:** 11 April 2026 | **Accepted:** 15 April 2026

Keywords: bimodal microstructure | composite precipitate assemblies | in situ scanning electron microscope compression | Ni-based superalloys | precipitate shearing

ABSTRACT

Inconel 718 is a Ni-base superalloy widely used in turbine disk components due to its excellent strength derived from the high volume fractions of γ″ precipitates. However, a transformation of γ″ to δ phase at elevated temperatures (700°C–900°C) restricts its use. To address this, a polycrystalline Ni–Cr–Al–Nb alloy was developed by optimizing Al:Nb ratio to increase the precipitate volume fraction. In this study, a bimodal microstructure was developed through controlled annealing, in which γ″ precipitates heterogeneously nucleated on γ′ precipitates, forming composite precipitate assemblies with coarse and fine distributions, as revealed by atom probe tomography (APT). In situ scanning electron microscope (SEM) micropillar compression tests exhibited a remarkable room-temperature strength of 1370 MPa and retained a strength of 1150 MPa at 773 K, indicating that the bimodal distribution effectively impedes dislocation motion. Precipitate shearing was found to be the dominant strengthening mechanism, irrespective of precipitate size, as identified by *postmortem* transmission electron microscope (TEM) analysis. The deformation pathway, determined using atomic-resolution high-angle annular dark-field (HAADF)–scanning transmission electron microscopy (STEM), was an intrinsic stacking fault (ISF) in γ″ coupled with a superlattice ISF (SISF) in the γ′ phase.

1 | Introduction

Inconel 718 (IN718) is a Ni-based superalloy used in the aerospace industry for jet engine turbine disks [1]. These nickel–chrome-based alloys were primarily designed to enhance oxidation resistance, but they are well known for their excellent creep resistance. The addition of elements like Al, Nb, Ti, etc., enhances strength because of the formation of the $L1_2$ ordered γ′-Ni_3Al and γ″-Ni_3Nb (Strukturbericht notation: DO_{22}) precipitates in the γ matrix during controlled annealing processes [2, 3]. Depending on the composition of the alloys and heat treatment, variations in precipitate size, distribution, and morphology can be achieved, which influence the yield strength and creep properties of the alloy. As modern gas turbines operate at progressively higher temperatures to achieve greater thermal efficiency and lower CO_2 emissions, there is an increasing demand for Ni-based superalloys with enhanced creep resistance and microstructural stability at elevated temperatures. However, IN718 alloys are restricted to service temperatures of below approximately 650°C [1] owing to the transformation of γ″ phase to its stable δ phase, which degrades the mechanical properties of the alloy.

Therefore, significant efforts have been made to improve the strength of these alloys by variations in heat-treatment routes [4–7] or by compositional changes [2, 3, 8]. Using temperature–time–transformation (TTT) diagrams, tailored heat treatment can be designed to modify precipitate distributions and morphology, improving mechanical response. For instance, the two-step annealing treatment [4–7] forms compact coprecipitates, where all six {100} facets of γ′ precipitates are covered by γ″ phase,

thereby, enhancing coarsening resistance compared to their monolithic forms. A dual-lobed or hamburger morphology, where a cuboidal γ′ phase is sandwiched between γ″ phase, was also reported [9], with improved creep resistance. Owing to their arrangement, we referred to them as composite precipitate assemblies (CPA) in this article.

Extensive research has been conducted to understand the deformation mechanisms of γ′ and γ″ precipitates. The γ′ precipitates are sheared by pairs of $\frac{a}{2}\langle 110\rangle$ superpartial dislocations, where the first dislocation creates an antiphase boundary (APB), and the second restores the $L1_2$ structure [10]. For γ″, shearing involves a group of dislocations—either doublets or quadruplets $\frac{a}{2}\langle 110\rangle$—dislocations to restore order in all three variants of the BCT structure [11, 12]. When acting together, this forces the dislocation through high-energy pathways and creates stacking fault configurations after shearing, which require high stresses. From the offset at the atomically flat interface between γ′ and γ″ phases, the shearing can be identified [13]. For γ″ sizes below 10 nm (whether monolithic or CPA), deformation primarily occurred on the (111) plane by partial dislocations, which shear the CPA, leaving planar faults behind [14, 15]. Recent studies provided detailed mechanistic insight into the deformation behavior of CPA in IN718 alloys [7, 13, 15]. Atomic-resolution high-angle annular dark-field–scanning transmission electron microscopy (HAADF–STEM) observations revealed that the most common configurations of the planar faults are $ISF_{\gamma''}$/$APB_{\gamma'}$/$ISF_{\gamma''}$ and $ISF_{\gamma''}$/$SISF_{\gamma'}$/$ISF_{\gamma''}$, which were further supported by phase-field modeling [13]. Though precipitate shearing emerged as the dominant deformation mechanism, the dislocation type, fault structures, and coupling behavior vary with alloy composition, heat treatment, and deformation conditions. For instance, increasing Nb enhances coherency strengthening via γ″ precipitates [16] and stabilizes the DO_{22} structure, yielding a higher APB energy than γ′. This leads to APB-like faults during shearing, which transform into stable ISFs that drive the formation of loops at the γ′/γ″ precipitate interface [17]. The addition of Ti [2, 8] retards the coarsening of γ″ precipitates, thereby delaying the transformation to the δ phase and improving thermal stability.

As one approach to overcome the limitations of IN718 prototypes, Ni–Cr–Al–Nb (NiCrAlNb) alloys have been systematically developed to achieve comparable volume fractions of both phases, resulting in excellent strength and thermal stability [18]. Al:Nb ratio governs the volume fractions of γ′–γ″ precipitates, for instance Al:Nb ratio of 0.67 dramatically increased the γ′ volume fraction to approximately 25% after ageing at 700°C for 1000 h [19]. Furthermore, the γ″→δ transformation was substantially delayed in these alloys—the δ phase appeared only after 500 h of annealing at 800°C, whereas it typically forms within 1 h in commercial IN718 alloys. The high volume fraction of γ′ phase kinetically suppresses the transformation of γ″ to δ [18, 20]. Although the transformation is unavoidable over extended periods at elevated temperatures, these alloys exhibit superior stability compared to commercial IN718 alloys.

Building on these findings, the present study aims to further enhance the mechanical properties and thermal stability of NiCrAlNb alloys. Through an optimized heat treatment process, a bimodal microstructure of γ′/γ′′ was developed, which consists of both coarse and fine CPA. Using advanced electron microscopy along with atom probe tomography (APT), the distribution and composition of these precipitates in the microstructure were studied. Furthermore, using high-temperature in situ scanning electron microscope (SEM) micropillar compression tests, the yield strength at 300 and 773 K was evaluated. Owing to its unique bimodal microstructure, the alloy exhibited promising strength exceeding previously reported values, which highlights the critical role of the bimodal CPAs. The correlation between microstructure and mechanical performance indicates that the dominant strengthening mechanism is precipitate strengthening.

2 | Experiments

NiCrAlNb alloy with nominal composition of Ni–15Cr–4Al–6Nb (in at.%) was arc melted on a water-cooled copper hearth under a high-purity argon atmosphere. The elements were procured from Sigma Aldrich with 99.99% purity. The melted button was remelted 3–4 times to obtain a homogeneous composition. The NiCrAlNb alloy was homogenized at 1200°C for 4 h, followed by water quenching to minimize element segregation. After homogenization, ageing at 800°C for 100 h followed by furnace cooling to obtain γ′–γ″ CPA in γ matrix. The selection of a heat treatment at 800°C for 100 h is based on the precipitation kinetics of γ′–γ″ phases, and the mechanical response reported in an earlier study [21]. According to the T–T–T diagram for NiCrAlNb alloy, at 800°C, γ″ precipitates nucleate and grow efficiently, and the hardness value reported after 100 h was 440 HV. The reported hardness after peak-ageing (10 h) at 800°C was 450 HV, therefore, in the present case, it is marginally overaged. Since the γ″ precipitates are metastable and eventually transform to the δ phase, this transformation requires a duration of ∼500 h (400 HV). The melted button was sectioned using a low-speed cutting machine (Isomet, Buehler). The sectioned samples were polished using SiC abrasive papers up to 4000 grit, followed by electropolishing (Struers LectroPol 5). A2 electrolyte at 20 V for 25 s, and a flow rate of 20 was used. The microstructure examination of electro-polished samples was conducted using a focused ion beam (FIB) –SEM dual-beam microscope (Crossbeam 550L, Zeiss). For crystallographic orientation analysis, an electron backscatter diffraction (EBSD) system (Symmetry S2, Oxford Instruments) attached to the FIB (Crossbeam 550L, Zeiss) was used at an acceleration voltage of 20 kV and a current of 2 nA. The number density and size of the precipitates were measured from a {100} oriented grain using ImageJ software. Around 250 precipitates were considered to determine the size of the precipitates. The composition of different precipitates was determined from APT using a LEAP 4000X HR (Cameca). The needles were run in laser mode at 40 K, with a pulse repetition rate of 125 kHz, a laser pulse energy of 60 pJ, and a target detection rate of 1.0%. IVASTM 3.8.4 software was used for reconstruction.

For micromechanical testing, the micropillars of diameter 1 μm, keeping an aspect ratio of 2–3, were fabricated using Ga^+ FIB (Crossbeam 550L, Zeiss) in a ⟨324⟩ oriented grain to promote single slip deformation. The milling was carried out in three sequential stages, all at 30 kV, using currents of 7 nA, 1.5 nA, and finally 700 pA. The taper angle was measured to be 3–4°.

In situ micropillar compression at room temperature (300 K) and at high temperature (773 K) was performed in a SEM (Zeiss Merlin Gemini II) using a Hysitron PI89 indenter (Bruker) in a displacement-controlled mode at a strain rate of $10^{-3}\,s^{-1}$. The load transducer has a maximum capacity of 500 mN and

a noise floor of 5 μN. A 2 μm flat punch made of diamond (Synton MDP) was used to test the micropillars at 300 K, while a tungsten carbide tip was used to test at high temperatures. For high-temperature tests, both the flat punch and the sample were heated independently at a rate of 10°C/min. To ensure both the sample and the flat punch were at the same test temperature (±0.1 K) and that there was no heat flow between them, a contact was made before testing. At each condition, 8–10 micropillars were tested. Engineering stress was calculated based on the top diameter of the pillar, and the yield stress was estimated at a 2% of the offset stress.

SEM imaging after testing was conducted to analyze the activated slip system during compression. STEM–HAADF was employed to determine the size and morphology of γ′–γ″ precipitates using the probe corrected transmission electron microscope (TEM; Themis 300, Thermo Fisher Scientific) operated at 300 kV. The electron-transparent TEM lamella was fabricated using Ga^+ FIB by the standard lift-out method from the deformed micropillars. The interactions between dislocations and CPA in the deformed micropillar were studied using TEM in annular bright-field (ABF)–STEM and HAADF–STEM modes. The STEM intensity maps were generated using custom Python scripts that identified atomic columns via local peak detection. The integrated column intensities were then normalized and spatially mapped to generate a continuous field representing relative atomic column contrast. EDS elemental maps were acquired using a super-X detector in STEM nanoprobe mode.

3 | Results

3.1 | Microstructure Characterization

Figure 1a shows the SEM image of the γ–γ′–γ″ microstructure from the ⟨001⟩ oriented grain in the NiCrAlNb heat-treated alloy. The γ′ precipitates are cuboidal in shape, whereas γ″ appeared as long needles due to an edge-on view of their disc-shaped morphology. The two orientations of γ″ are identified in this viewing direction, corresponding to their orientation relationship with γ′ precipitates. It has been known that γ′ precipitates formed first in the γ matrix and act as heterogeneous nucleation sites for γ″ precipitates [2, 22, 23]. The orientation relationship between γ′ and γ″ precipitates was reported to be: $\{100\}_{\gamma'} \| \{100\}_{\gamma''}$; therefore, two variants are visible in the ⟨001⟩ oriented grain.

To verify the bimodal distribution of precipitates, TEM analysis was performed on the aged NiCrAlNb alloy. Figures 1b–e and 2 show a representative analysis from a [110]-oriented grain. The corresponding diffraction pattern (Figure 1b) exhibits

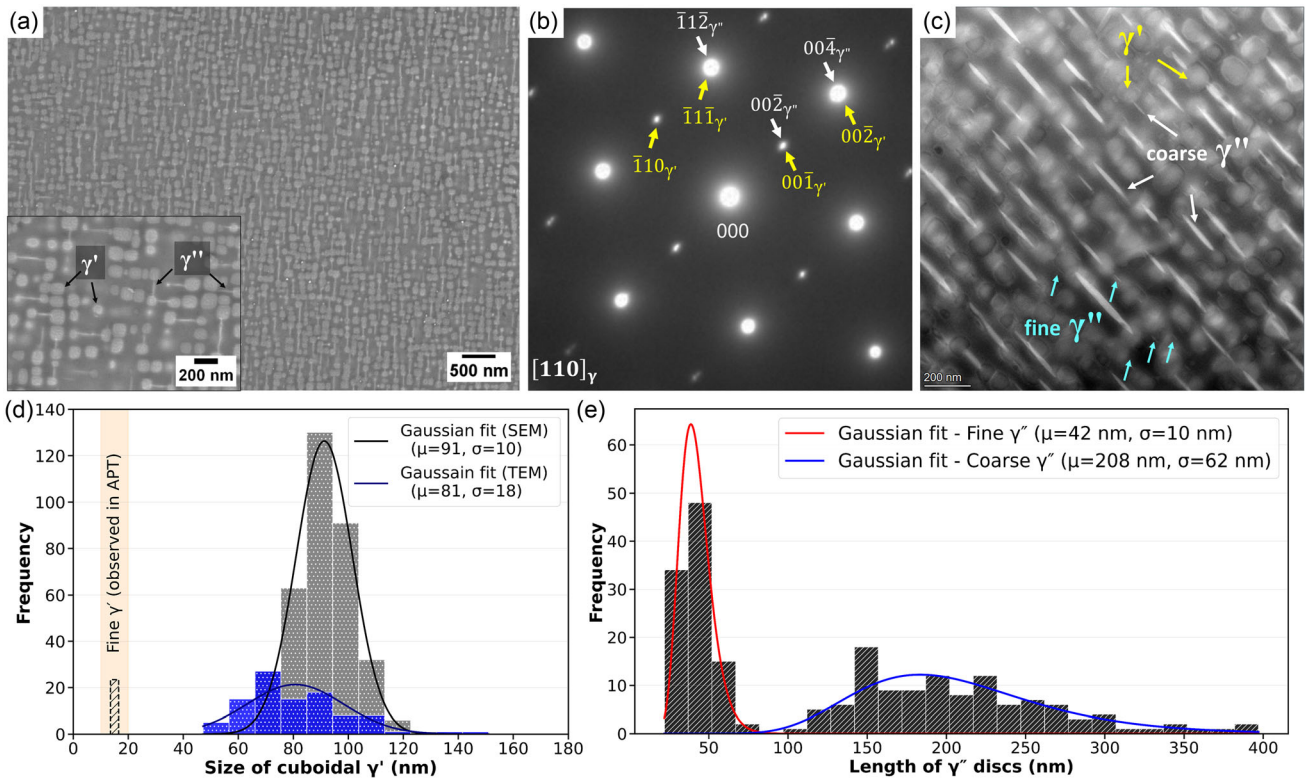

FIGURE 1 | (a) SEM image from ⟨001⟩ oriented grain showing γ–γ′–γ″ microstructure in the aged NiCrAlNb alloy. The inset is a high-magnification view illustrating the cuboidal γ′ precipitates and two variants of disc-shaped γ″ precipitates. The γ″ precipitates viewed edge-on, resulting in their needlelike appearance, consistent with their formation on the {100} planes of γ′ precipitates. TEM analysis from a [110] oriented grain. (b) Selected area diffraction pattern showing superlattice spots corresponding to γ′ precipitates (yellow arrows) and γ″ precipitates (white arrows). (c) HAADF–STEM image showing coarse and fine γ″ precipitates (appear bright in contrast due to their Nb content) alongside γ′ precipitates. (d) Histogram of cuboidal γ′ precipitates measured from SEM and TEM images. The Gaussian fits to the SEM and TEM data yielded mean sizes of 91 ± 10 and 81 ± 18 nm, respectively. A hatched bar and shaded region indicate the presence of fine γ′ precipitates (10–20 nm in size) observed in APT measurements. (e) Length distribution histogram of γ″ precipitates showing bimodal distribution, giving a mean length of coarse precipitates as 208 ± 62 nm, and for fine precipitates as 42 ± 10 nm (from Gaussian fitting).

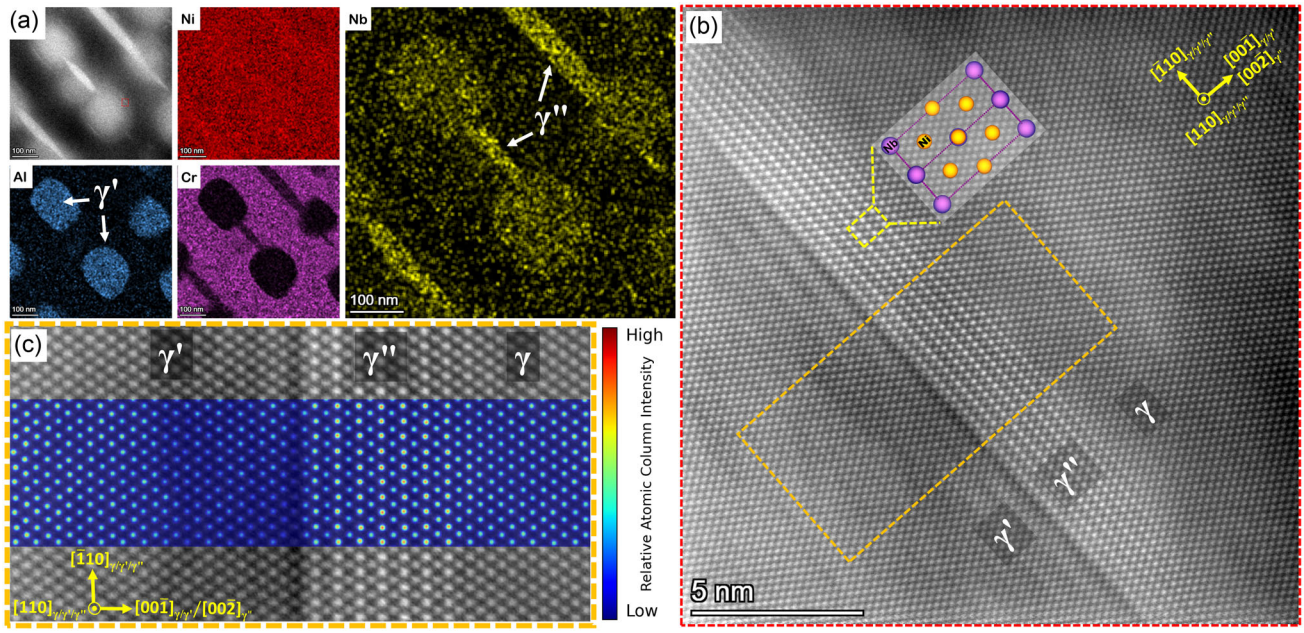

FIGURE 2 | TEM analysis of the aged NiCrAlNb alloy from a [110] oriented grain. (a) STEM–EDS elemental maps at high resolution showing coarse γ″ precipitates (rich in Nb) and γ′ precipitates (rich in Al). (b) Atomic resolution HAADF–STEM image acquired at the interface of γ′/γ (red outline in (a)), revealing the presence of fine γ″ precipitates at the interface of γ′ precipitate. The inset shows the atomic arrangement in γ″ phase in [110] orientation and (c) high magnification atomic resolution HAADF–STEM image from the region marked by orange outline in (b), overlaid with corresponding STEM intensity maps, showing the mixed atomic columns of the γ′, characteristic alternate Nb-rich atomic columns of the γ″ phase, and Ni atomic columns of γ. A low-intensity atomic plane corresponds to a localized Al-rich interfacial layer at γ′/γ″ interface is observed. The post-processing to generate the STEM intensity map was performed using custom Python scripts.

superlattice spots consistent with γ′ precipitates (yellow arrows) and γ″ precipitates (white arrows). Both γ′ and γ″ precipitates were captured in the low magnification HAADF–STEM image (Figure 1c). Quantitative analysis yielded a mean diameter of 81 ± 17 nm for the γ′ precipitates in the TEM data, while 91 ± 10 nm from the SEM data (Figure 1d). Coarse and fine γ″ precipitates exhibited average lengths of 208 ± 62 nm and 42 ± 10 nm, respectively (Figure 1e). STEM–EDS elemental maps in Figure 2a further help identify the precipitates, and the measured compositions are summarized in Table 1. Fine γ″ precipitates, which were not clearly resolved in Figure 1b, were examined by atomic resolution HAADF–STEM near the interface of γ′ precipitates. As shown in Figure 2b, the fine γ″ precipitates were evidently resolved. The high magnification image in Figure 2c, overlaid with a STEM intensity map, reveals the characteristic alternate Nb-rich atomic columns of the γ″ phase. These observations confirm a bimodal distribution of precipitates in the γ matrix.

The reconstructed atom map of the NiCrAlNb heat-treated alloy obtained by APT is shown in Figure 3a. The 3D visual of the APT tip is provided in Supporting Video 1. In addition to the coarse cuboidal precipitates with a size of several tenths of nanometers

TABLE 1 | Summary of the composition (at.%) of all elements in the γ matrix, cuboidal γ′ and plate-like γ" precipitates obtained from APT and STEM–EDS. The error represents the standard deviation obtained from the line profiles.

Method - APT					
Elements	**Coarse cuboidal**	**Fine cuboidal**	**Coarse plate**	**Fine plate**	**Matrix**
Phase	γ′	γ′	γ″	γ″	γ
Ni	74.9 ± 1.2	73.3 ± 2.9	74.8 ± 0.9	74.7	72.4 ± 0.5
Cr	6.4 ± 0.6	7.3 ± 1.7	6.9 ± 0.6	7.4	23.8 ± 0.5
Al	9.5 ± 0.8	10.3 ± 2.0	1.3 ± 0.2	1.0	0.3 ± 0.1
Nb	9.2 ± 0.8	9.1 ± 2.2	17.0 ± 0.8	16.9	3.5 ± 0.2
Method - STEM–EDS					
Ni	75.0 ± 1.6	—	76.0 ± 0.4	70.0 ± 2.9	73.2 ± 2.1
Cr	3.2 ± 0.7	—	7.8 ± 0.2	10.0 ± 1.2	21.6 ± 1.7
Al	15.0 ± 1.8	—	2.5 ± 0.2	2.4 ± 0.2	2.6 ± 0.8
Nb	6.9 ± 1.2	—	13.7 ± 0.4	17.6 ± 2.5	2.6 ± 1.0

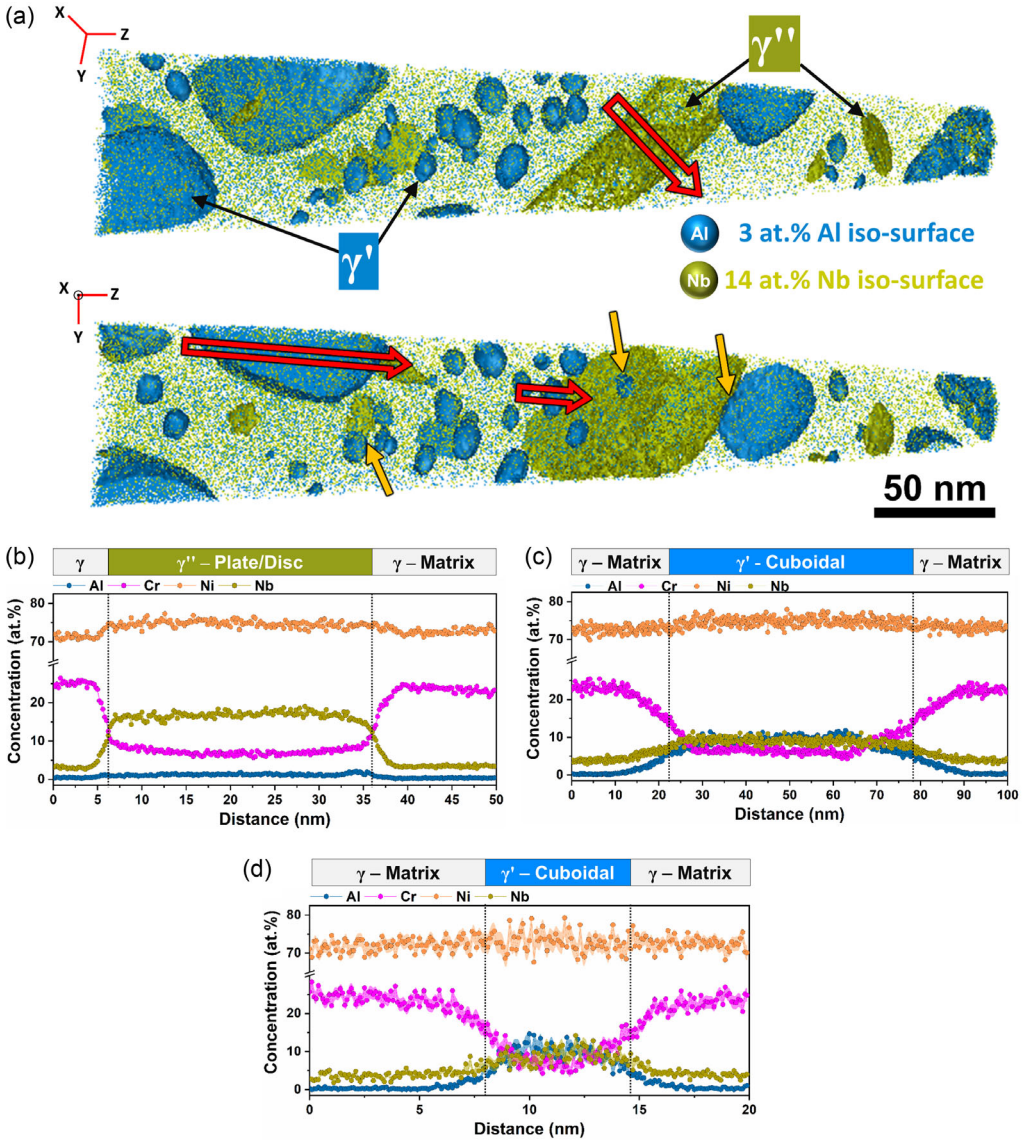

FIGURE 3 | APT analysis of the NiCrAlNb alloy after ageing at 800°C for 100 h. (a) Three-dimensional (3D) APT reconstruction showing Al (blue) and Nb (green) atom distributions. Iso-concentration surfaces at 3 at% Al and 14 at% Nb delineate the γ matrix, Al-rich cuboidal γ′ precipitates, and Nb-rich disc-shaped γ″ precipitates. The orange arrow indicates the heterogeneous nucleation of γ″ precipitates on γ′ precipitates. One-dimensional (1D) proximity histograms showing compositional profiles across (b) a γ″ plate, (c) a coarse γ′ precipitate, and (d) a fine γ′ precipitate. The red arrow indicates the analysis direction for each profile.

(or larger) as observed in the SEM images, several fine precipitates were also observed in certain regions in the 3D atom map. From the 3D atom map, disc-shaped morphology of γ″ precipitates was revealed, and due to their edge-on orientation in ⟨001⟩ orientation, they appeared as needles in the SEM/TEM images. Further, these disc-shaped precipitates were also heterogeneously nucleated on fine cuboidal precipitates (marked by orange arrows in Figure 3a). Further, the 3D atom map confirms the bimodal microstructure of γ′ precipitates, which was not clearly distinguishable in the HAADF–STEM image due to overlapping contrast in Figure 1c. Consequently, quantitative size analysis of these fine precipitates is challenging; however, APT reveals that they are approximately 10–20 nm in size (Figure 1d).

The composition of these precipitates was determined and is presented through 1D composition profiles in Figure 3c,d. The average compositions, calculated from multiple precipitates, were summarized in Table 1. The solubility of Cr was higher than Al in γ″ plate precipitates, which was consistent with the literature [24]. The plate precipitate stoichiometry can be inferred from its composition and could be $Ni_3(Nb, Al,Cr)$, with an approximate Nb/(Al + Cr) atomic ratio of 2. In contrast, the γ′ cuboidal precipitates, regardless of their size, exhibit a consistent composition corresponding to a stoichiometry of $Ni_3(Al, Nb,Cr)$, with an Al/(Nb + Cr) atomic ratio of approximately 0.6, where Al content is nearly equal to Nb.

3.2 | In Situ SEM Micropillar Compression

A ⟨324⟩ oriented grain was selected for in situ mechanical testing, and displayed in the EBSD inverse pole figure (IPF) map in the Z-direction as in Figure 4a. This orientation was chosen to ensure the activation of the single slip system with the highest Schmid

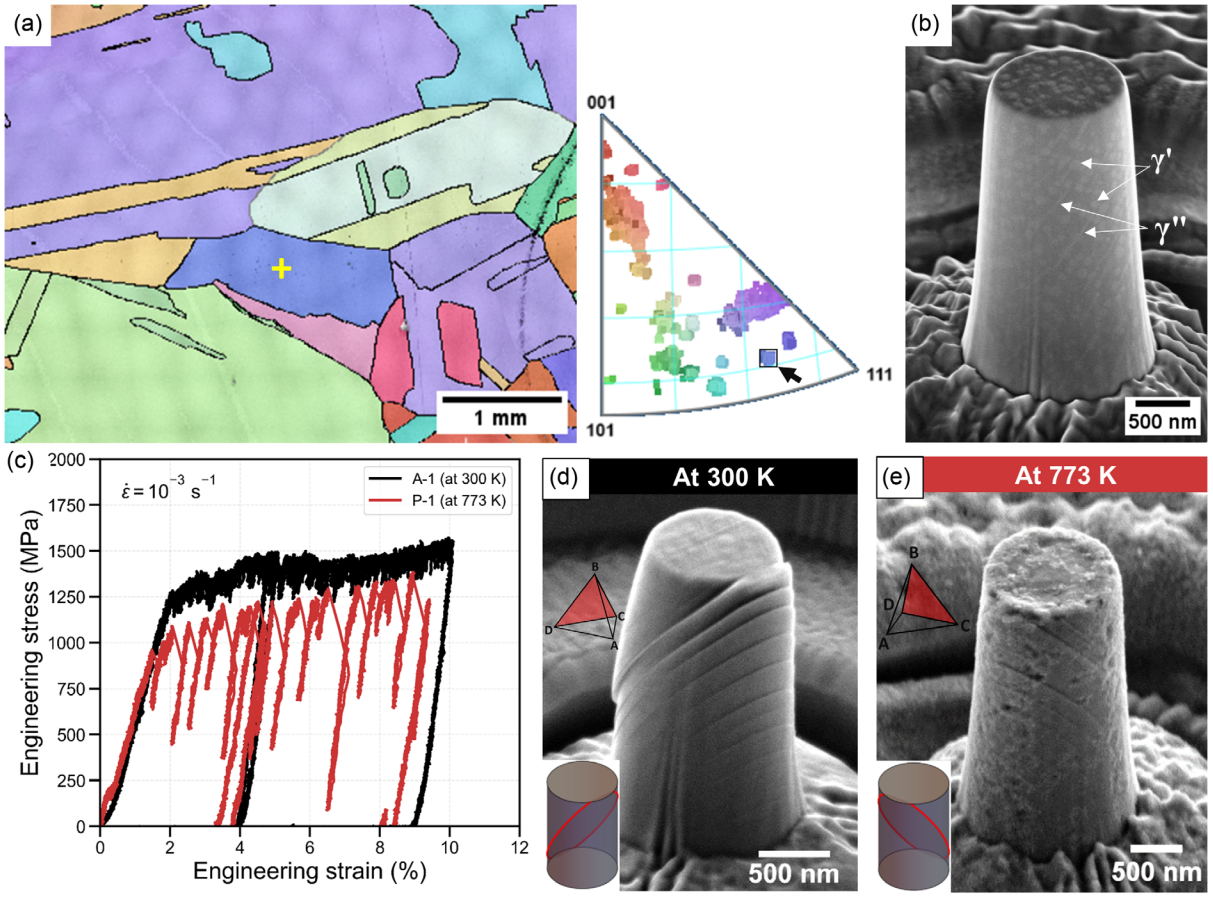

FIGURE 4 | (a) Inverse pole figure (IPF)-Z maps showing the grain structure. The "+" sign indicates the ⟨324⟩ oriented grain selected for micropillars fabrication, and (b) SEM image using an in-lens detector of a micropillar resolving the γ′-γ″ precipitates within it. (c) A representative stress–strain curve from an in situ SEM deformation test at 300 and 773 K of a micropillar in ⟨324⟩ oriented grain in NiCrAlNb alloy, (d) a representative *postmortem* SEM image of the deformed micropillar tested at 300 K, showing slip traces with simulated pillar and Thompson tetrahedron in the inset, and (e) a representative *postmortem* SEM image of the deformed micropillar tested at 773 K, with visible slip traces and surface oxidation. The inset shows the simulated pillar and Thompson tetrahedron.

factor (in this case, $[011](1\bar{1}1)$ and $m = 0.40$) under uniaxial compression loading. This approach was implemented to simplify the interpretation of the mechanical response and the deformation behavior, particularly with respect to the dislocation–CPA interaction. The SEM image of the fabricated micropillar was acquired using an in-lens secondary electron detector, which helped locate the γ′ and γ″ precipitates within it (Figure 4b).

The representative stress–strain curve from a micropillar in ⟨324⟩ oriented grain tested at 300 K under a 10^{-3} strain rate is shown in Figure 4c. Loading was stopped after 10% strain. Additionally, the load function is split into 5% and 5% strain to reduce lateral forces and ensure uniform deformation. The stress–strain curves from seven different micropillars tested at 300 K are shown in Figure S1. The representative *postmortem* SEM image in Figure 4d shows the multiple activation of a single slip system. The simulated micropillar in the inset of Figure 4d, in the same orientation as the SEM image, highlighted the activated slip plane $(1\bar{1}1)$ in red color, as expected from the Schmid factor calculation.

Next, in situ compression tests were conducted at 773 K at a strain rate of 10^{-3}. The stress–strain curve in Figure 4c suggests a decrease in yield strength compared to 300 K tests. Individual stress–strain curves for all micropillars tested under similar conditions are available in Figure S2. The yield strength was estimated by taking 2% offset stress with an unloading stiffness. The cumulative distribution function (CDF) plot in Figure 5 shows a decrease in yield strength of 210 MPa at 773 K. Based

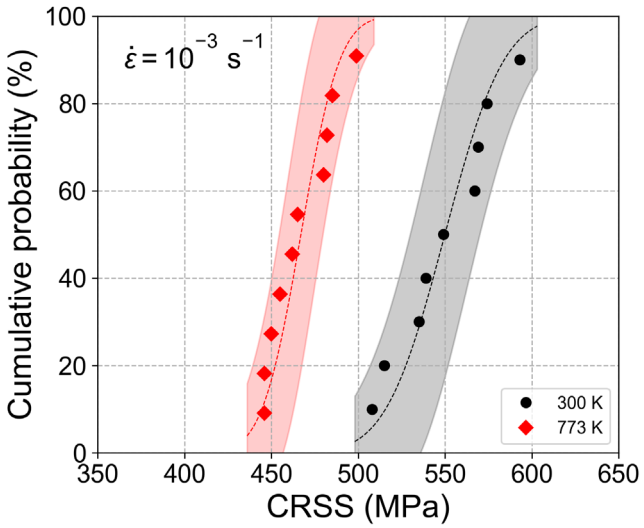

FIGURE 5 | Cumulative distribution function (CDF) with 95% confidence index of yield strength (2% proof stress) of micropillars tested at 300 K and 773 K.

on the loading direction from EBSD, the critical resolved shear stresses (CRSS; CRSS = $m \times$ yield strength) were estimated to be 550 ± 28 MPa at 300 K and 467 ± 18 MPa at 773 K.

The surface oxidation occurred during high-temperature tests, which was visible in the *postmortem* SEM image, in Figure 4e, along with the slip traces of the activated slip plane. Since oxidation in these alloy systems follows a parabolic growth law, the tests were limited to 773 K to avoid the effects of oxides on the mechanical data.

Noteworthy is that an increase in the magnitude of the load drops was observed in the stress–strain curves at 773 K. This behavior is attributed to a synergistic interplay of thermally activated processes, such as dislocation cross-slip [25, 26]. It suggests that the CPAs, which are expected to be a strong barrier to dislocation motion at low temperatures, become less effective at 773 K, providing an easier path for dislocations to glide and for strain bursts to form.

3.3 | *Postmortem* TEM investigations

The ABF–STEM (collection angle 8–30 mrad) and HAADF–STEM (collection angle 30–200 mrad) images in Figure 6 were acquired from the deformed micropillar at 773 K (strain up to 10%), along $[\bar{1}\,\bar{1}\,0]$ zone-axis (CD direction in Thompson notation).

The SAED pattern, in Figure S3a, exhibits the superlattice spots corresponding to γ′-γ″ precipitates. The γ′ precipitates are rotated by 45° about the c-axis in this zone-axis condition, as shown in Figure S3b. The activated slip plane $(1\bar{1}1)$, or BCD plane in the Thompson tetrahedron is edge-on in this orientation, as shown in the inset of Figure 6a. Due to the presence of the dislocations on the activated slip plane $(1\bar{1}1)$, and that being edge-on in this zone-axis condition, the slip traces were easily identified and indicated by white arrows. They appear dark contrast in ABF-STEM image (Figure 6b–f) and bright in HAADF–STEM

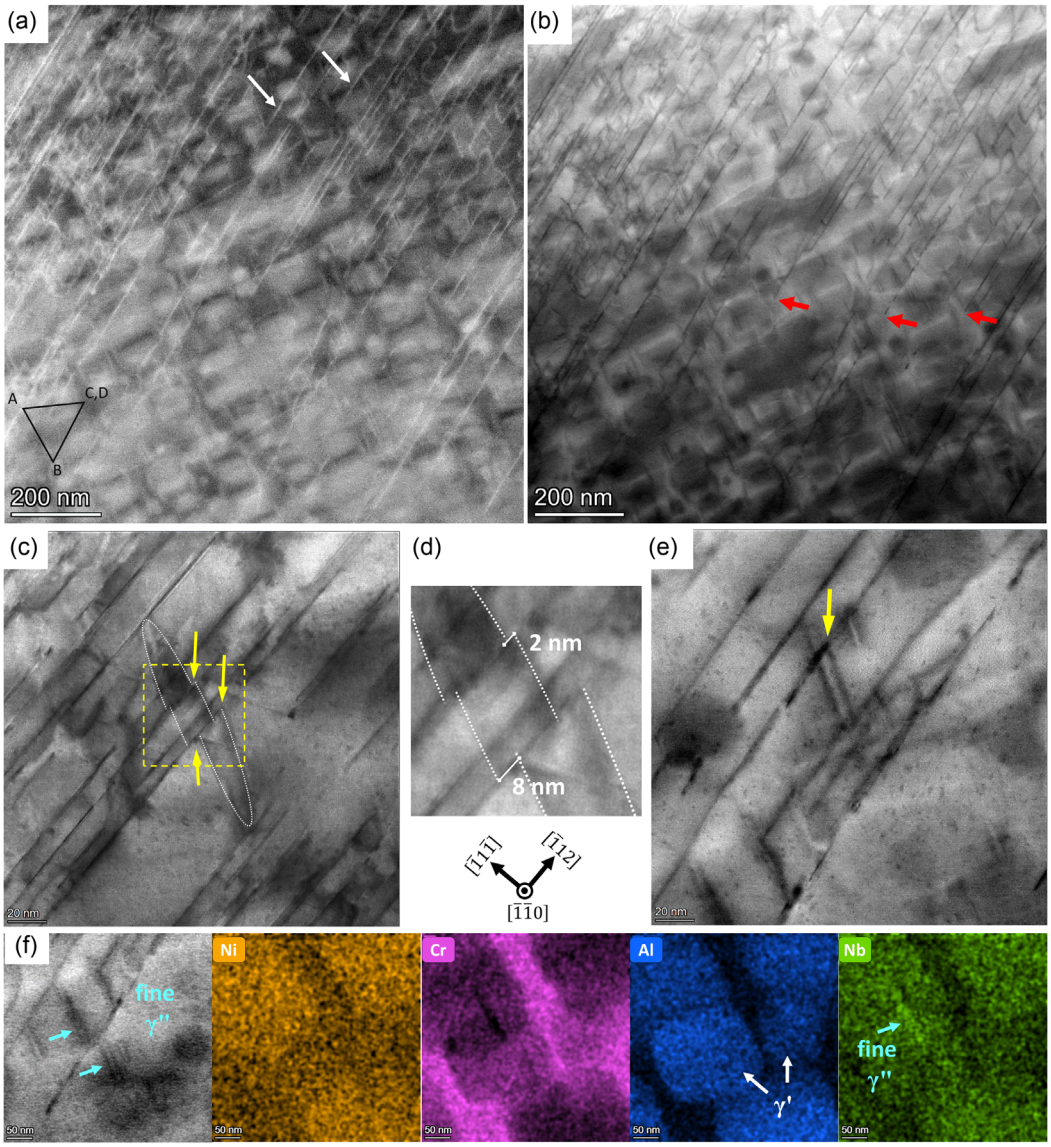

FIGURE 6 | TEM analysis of deformed micropillar (up to 10% strain) at 773 K along $[\bar{1}\,\bar{1}\,0]$ zone-axis. (a) HAADF–STEM image (collection angle: 21–125 mrad), (b) corresponding ABF–STEM image (collection angle: 5–19 mrad) showing traces of activated slip planes (white arrows) and evidence of the termination of slip traces in the γ′ precipitates (red arrows). The inset in (a) shows the Thompson tetrahedron in this zone-axis condition. High magnification ABF–STEM images showing (c) shearing of coarse γ″ precipitate, (d) offset between upper and lower segments of γ″ precipitate, and (e) shearing of fine γ″ precipitate. (f) ABF–STEM image and STEM–EDS maps of all elements showing γ′ and γ″ precipitates in the deformed micropillar.

(Figure 6a) due to the localized lattice distortions from the presence of dislocation on the activated slip plane. Dislocation glide in Ni-based superalloys leads to the formation of various planar faults, which may contribute to the contrast observed in STEM images. These planar faults on the activated slip plane were observed in another deformed micropillar at 773 K when viewed along $[\bar{1}10]$ zone-axis, in Figure S4. The STEM-EDS maps of all elements in Figure 6e clearly reveal the γ' precipitates (Ni enrichment) and the fine γ'' precipitates (Nb enrichment and Cr depletion).

The presence of multiple slip traces passing through the γ' and γ'' precipitates, regardless of their size, indicates that the precipitates are sheared (Figure 6c). At the slip traces, the precipitate shows a measurable offset between its upper and lower segments (yellow arrows in Figure 6c–e), indicating a shearing event. Further, in coarse γ'' precipitates, multiple shearing was evident (Figure 6c–d) and a maximum offset of ~8 nm was measured. To understand the shearing mechanism, atomic-resolution STEM imaging was performed. Atomic resolution HAADF–STEM image in $[\bar{1}\,\bar{1}\,0]$ zone axis with $(1\bar{1}1)$ activated slip plane oriented edge-on, enabling direct visualization of the fault plane (Figure 7). The fault in the γ'' precipitates was characterized by alternating Nb-rich atomic columns in the γ'' phase in this orientation. The projected shift of 0.14 nm was measured along the $[\bar{1}12]$ direction. The theoretical magnitude of a Shockley partial dislocation vector corresponding to an intrinsic stacking fault (ISF, $\frac{a}{6}\langle 112\rangle$) is 0.148 nm ($a = 0.362$ nm for γ''-Ni_3Nb phase). Our experimentally measured displacement is in close agreement with the ISF. In contrast, a superlattice ISF (SISF; $\frac{a}{3}\langle 112\rangle$) would require a displacement of 0.296 nm, comparatively larger than the measured value. Lv et al. reported the first-principles generalized stacking fault (GSF) energy calculations for γ''-Ni_3Nb phase (DO_{22}) [17]. Based on these energetics, ISFs (2.3 mJ/m^2) were energetically more favorable than SISFs (613 mJ/m^2), supporting our experimental observations.

The shearing of γ' precipitates was also by the stacking faults, which were resolved from the atomic-resolution HAADF–STEM image (Figure 8). Since the atomic Z contrast is not as clear as in γ'' precipitates (Figure 7), the superlattice spots in the FFT (inset of Figure 8a) confirmed it to be γ' precipitates. The stacking faults were found to be intrinsic in type (magnified image near the fault complemented with the STEM intensity map). However, it is difficult to determine if it is a complex (CISF) or a SISF in this orientation (refer to Figure 1 in [27]). Following the energy criterion, SISF is much lower than CISF [10]; therefore, it is reasonable to assume that the fault is SISF. Further, high-magnification images reveal that most slip traces terminate at γ' precipitates (marked by red arrows in Figure 6b). It indicates the dislocations were arrested in this phase, suggesting it to be the dominant strengthening phase, compared to the γ'' precipitates. Using the atomic resolution HAADF–STEM image near the γ''/γ' interface and the corresponding Bragg-filtered image constructed from $(\bar{1}11)$ reflection, in Figure 8b, identifies the terminating end of an intrinsic fault within γ' precipitates on the $(1\bar{1}1)$ plane.

To observe the dislocations, the specimen was tilted away from the edge-on condition to view the activated slip plane and dislocation–precipitate interactions within the slip plane, from $[\bar{1}\,\bar{1}\,0]$ zone axis to $[\bar{1}\,\bar{3}\,0]$ zone axis (Figure 9a). ABF–STEM image (collection angle: 5–19 mrad) reveals the dislocations on the activated slip plane (Figure 9b). A high magnification image from the region where the slip was terminated, in Figure 9c, reveals the dislocation-precipitate interactions. It can be inferred that the dislocation is interacting with both γ'' and γ' precipitates. From the atomic-resolution HAADF–STEM images (Figure 8),

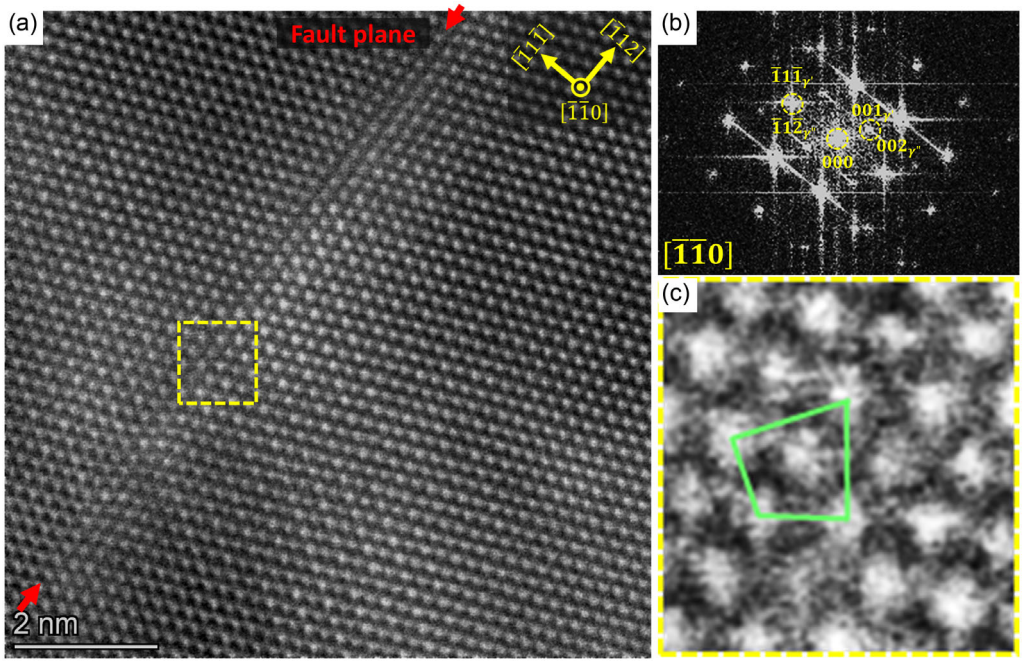

FIGURE 7 | (a) Atomic resolution HAADF–STEM image along $[\bar{1}\,\bar{1}\,0]$ zone axis showing the shearing of γ'' precipitate (identified using alternate Nb-rich atomic columns in γ''), (b) FFT confirming the superlattice spots corresponding to the γ'' precipitate, and (c) magnified view of the marked region in (a) showing the distortion (polygon unit) indicative of the ISF.

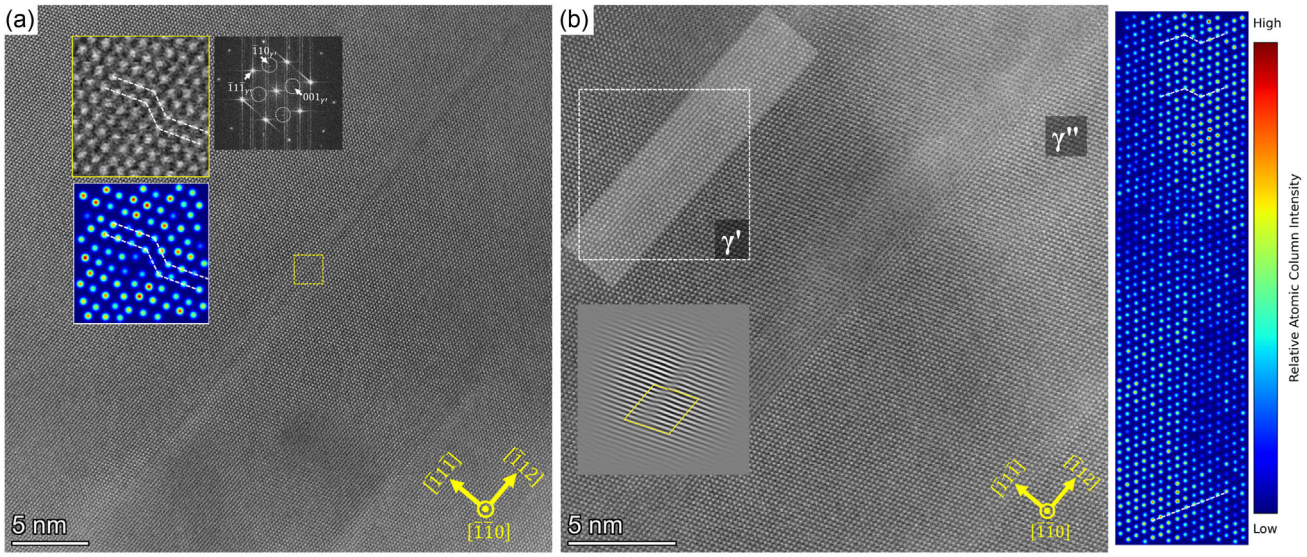

FIGURE 8 | Atomic resolution HAADF–STEM images along $[\bar{1}\,\bar{1}\,0]$ zone axis. (a) SISF within the γ′ precipitate. The inset shows a magnified view of the fault plane along with the STEM intensity map. The FFT (inset) confirmed the ordered γ′ phase. (b) Termination of the fault within the γ′ phase. The inset shows a Bragg-filtered image constructed using $(\bar{1}11)$ reflection, highlighted the faulted and perfect lattice regions. The stem intensity map from the shaded region further helps in visualizing the fault termination within the γ' precipitate.

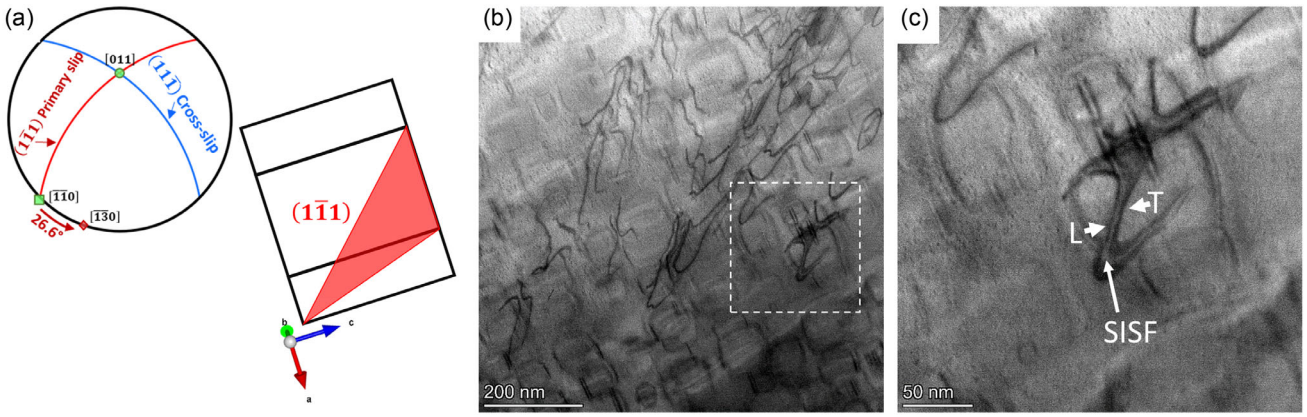

FIGURE 9 | (a) Stereographic projection along direction and schematic of the activated slip plane (inclined) inside a γ′ precipitate aligned in $[\bar{1}\,\bar{3}\,0]$ zone axis. ABF–STEM images (5–19 mrad) along $[\bar{1}\,\bar{3}\,0]$ zone axis: (b) dislocations on the activated slip plane and (c) high magnification image showing the dislocation interaction with γ″ and γ′ precipitates (L: leading dislocation, T is trailing dislocation, and SISF: superlattice intrinsic stacking fault).

it is clear that the precipitates undergo stacking fault shearing. The dislocation observed in the ABF–STEM image (Figure 9c) corresponds to the partial dislocations (Leading: L, and Trailing: T), and the shaded region between them corresponds to the stacking fault. Since the precipitate is not yet completely sheared by the dislocations, the bowing of the dislocation line can be observed.

In addition, curved dislocations were also observed located between the slip traces. Under this imaging condition, the dislocations, since they are confined to the activated slip plane, were not visible (Figure 10a). However, we observed the dislocation segments (curved) located between adjacent slip traces, and in most cases, connecting them (Figure 10b). The dislocations on (111) and $(11\bar{1})$ slip planes can be visible under this imaging condition, as these planes are inclined with respect to the beam condition, whereas the other two slip planes ($(1\bar{1}1)$ and $(\bar{1}11)$) are edge-on and therefore, dislocations cannot be resolved on them. Since the dislocations were resolved in ABF-STEM images, it is unlikely to be confined to the activated slip plane. This indicates that the dislocations were cross-slipped onto other slip-planes ((111) and $(11\bar{1})$). Further, since the Burger vector of dislocation is of type $\frac{a}{6}\langle 011\rangle$, the screw component enables cross-slip onto $(11\bar{1})$ plane, crystallographically more favorable than (111) plane (see Figure 9a).

4 | Discussion

The presence of γ′/γ″ CPA (hamburger or sandwich structures [13, 15, 28]) in IN718 or similar alloys is frequently observed because it reduces the total elastic energy compared to its monolithic forms. Their deformation is governed by the synergistic

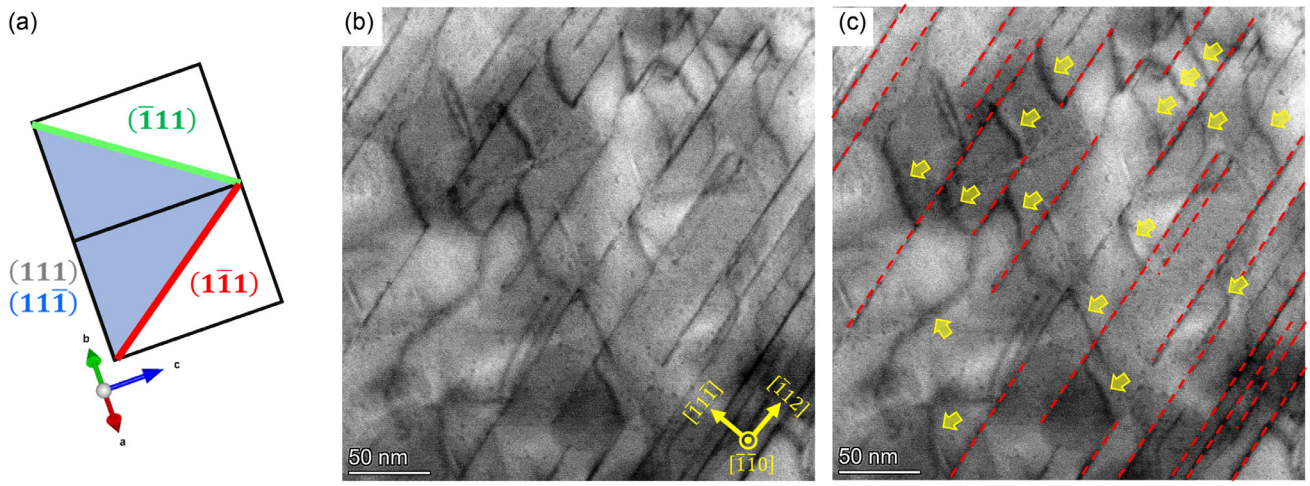

FIGURE 10 | (a) Schematic of the Thompson tetrahedron inside a γ′ precipitate aligned in $[\bar{1}\,\bar{1}\,0]$ zone axis. ABF-STEM images (5–19 mrad) along $[\bar{1}\,\bar{1}\,0]$ zone axis: (b) curved dislocations between the slip-traces of the activated slip plane, indicating cross-slip events during deformation and (c) same image as in (b) with the curved dislocation marked by yellow arrows and the activated slip plane by red dashed line for clarity.

interplay between $L1_2$ and DO_{22} symmetries, creating a unique pathway depending upon the Burger vector direction; for instance, a single $\frac{a}{2}\langle 110\rangle$ dislocation may create a stable APB in γ′ [10], but an unstable APB-like fault in γ″ [13, 17]. These unstable faults often transform to the low-energy stable ISF within γ″ [17]. The development of a bimodal distribution of CPA in the matrix is an effective strategy for further enhancing the yield strength of advanced alloys by activating multiple, synergistic strengthening mechanisms. The yield strength is approximately 15% higher compared to NiCrAlNb heat-treated alloys (700°C for 1000 h) with unimodal distribution of γ′ and γ″ precipitates, tested at 300 K from the same oriented grain at 10^{-3} strain rate (refer to Figure S5 of Supporting file). This provides direct evidence for the superior strengthening effect of the bimodal distribution of γ′ and γ″ precipitates in the γ matrix. In Ni-based superalloys, a bimodal distribution of γ′ precipitates—comprising fine secondary/tertiary $L1_2$-ordered precipitates with the coarse primary ones— often leads to an increase in strength, exceeding 1 GPa at room temperature. For instance, Zhang et al. achieved a remarkable strength of 1520 MPa in a peak-aged GH4720Li superalloy with a bimodal/trimodal distribution of the γ′ precipitates [29]. This is also reported in the work of Kumari et al. on ATI 718Plus alloy, which demonstrated a yield strength of ∼930 MPa [30]. The effect of bimodal distribution of precipitates is not limited to Ni-based superalloys but has been successfully applied in other systems, including CoCrNi medium entropy alloys (MEA) [31], Al-based alloys [32–34], Mg-based alloys [35], and Co-based superalloys [36, 37]. In CoCrNi MEA [31], a yield strength of 1.1 GPa has been attributed to the bimodal distribution of $L1_2$ order precipitates, while in Co-based superalloys, the presence of primary and secondary γ′ precipitates enhances the strength. In these reported cases, strengthening occurs primarily through APB shearing or stacking fault shearing, with a negligible contribution from the Orowan looping mechanism. Similarly, in the present study, direct evidence of precipitate shearing is observed (Figure 6). From the TEM analysis after in situ deformation at 773 K, the observed deformation pathways were: the low-energy ISF in γ″ couples with SISF in γ′.

The observations of stacking faults at atomic resolution indicate that the active deformation mechanism shifts from a traditional APB shearing governed by a unit $\frac{a}{2}\langle 110\rangle$ superpartial pairs to Shockley pairs of dislocations. In dual-phase precipitates, the transition from APB to SISF in the γ′ phase is driven by an incoming SISF dislocation of ultralow energy (∼2.3 mJ/m^2 [17]) in the γ″ phase propagating into the γ′ phase. A strengthening model for multimodal distribution of γ′ precipitates [38], based on weak-pair and strong-pair coupling of dislocations, indicates that the strengthening is governed by precipitate size, maximizing at the critical radius, which is intrinsically linked to the APB energy. Below the critical radius, weak-pair coupling dominates, allowing dislocations to fully shear the precipitates, whereas above it, strong-pair coupling prevails, where dislocations only partially penetrate the precipitates. The observation of slip traces terminating in the γ′ precipitates provides direct evidence that the dislocations are unable to shear the γ′ precipitates, indicating that γ′ precipitate deformation is governed by a strong-pair coupling mechanism. While in the present case, it deviates from the classical strengthening models based on APB formation, however, by utilizing SISF energy as the primary resistance rather than APB energy [13], the model can be adapted to rationalize the CRSS behavior. Qualitatively, our observation confirms that the γ′ precipitates are acting as strong, effective barriers to slip. Beyond the shearing of γ′ precipitates, the shearing was observed for γ″ precipitates across their diameter. The frequent shearing was noticed for the coarser ones. This aligns with findings by He et al. [39], who reported that a bimodal distribution of γ′ and γ″ precipitates in modified 955 Ni-based superalloy, particularly γ′–γ″ duplets and triplets, enhanced yield strength by ∼11%, compared to a unimodal distribution, with shearing being an active mechanism irrespective of the precipitate size.

To model the cumulative strengthening effect (σ_t) from these morphologically distinct precipitates (for instance: cuboidal γ′ and disc-shaped γ″ in Ni-based superalloys), a superposition

law was applied using a weighted root–mean square approach ($\sigma_t^\alpha = \sum_i f_i^\beta \sigma_i^\alpha$, where f is the volume fraction of precipitate, β and α are constants [40]). This model accounts for the pinning effects of precipitates (β) and their projections on the dislocation slip plane (α) and has been validated in systems like Al-based alloys [41, 42], containing spherical and disc-shaped precipitates. However, the quantitative prediction of strength in the present system is limited by several factors. The measured volume of coarse γ′ precipitates is ∼18%, consistent with the 19%–24% range reported for similar NiCrAlNb alloys aged at 700°C–800°C [18, 19]. In contrast, the volume fractions measured for fine and coarse γ″ precipitates (∼4% and 6%, respectively) are lower than the reported range of 20%–25% [18, 19]. The discrepancy in the present work is likely due to two experimental limitations: (i) the TEM analysis was conducted along the ⟨110⟩ zone-axis, may not accurately represent the true thickness of disc-shaped γ″ precipitates and (ii) random sectioning of γ″ discs by the foil plane, resulting in the observed diameter to be less than its true length. Additionally, the accurate strength prediction requires APB energy for both γ′ and γ″ precipitates at the experimental conditions. Nevertheless, following the superposition law ($\sum_i f_i^\beta \sigma_i^\alpha$), the strength can potentially be pushed further by synergistically increasing the volume fraction of strengthening γ′ phase, and maintaining its size near the critical range, where the transition from weak-pair coupling to strong-pair coupling occurs.

Next, the decrease in strength observed at 773 K (in Figure 4) can be attributed to the dislocation cross-slip process, evident in STEM images of the deformed micropillar at 773 K, enhances dislocation mobility and reduces the effectiveness of the barrier. While solid solution strengthening from the solutes in the matrix also contributes to the overall strength, its contribution is expected to remain unaffected at 773 K. Alterations in matrix composition, driven by either precipitate growth or dissolution, are unlikely under these experimental conditions. The test temperature of 773 K is low for diffusion-driven processes, as the growth of these γ″ precipitates is reported above 923 K (650°C), and the transformation of γ″ to the δ phase occurs during long-term ageing at 1073 K or above [18, 19, 43]. Furthermore, considering the test time spans only a few minutes, there was insufficient time for solute diffusion to alter the matrix composition.

5 | Conclusion

This study highlights that a bimodal distribution of γ′ and γ″ precipitates in the γ matrix is highly effective in enhancing the yield strength of NiCrAlNb alloy. The microstructure, developed through annealing treatment at 800°C for 100 h followed by furnace cooling, was characterized using electron microscopy and APT studies, which reveal the existence of γ′–γ″ CPA in a bimodal distribution. From the in situ micropillar compression test of micron-sized pillars, the average yield strength at 300 K was 1370 MPa, which decreases to 1150 MPa at 773 K. Postdeformation STEM images confirm that precipitate shearing is the primary strengthening mechanism, with terminated slip traces within γ′ precipitates providing direct evidence of dislocations being effectively blocked. The deformation pathway involves the formation of a low-energy ISF in γ″ coupled with SISF in γ′. The reduction in yield strength at 773 K is attributed to dislocation cross-slip.

Author Contributions

Ujjval Bansal: conceptualization, investigation, formal analysis, data curation, methodology, writing – original draft, writing – review & editing, funding acquisition. **TaeHyeok Kang**: resources, data curation, writing – review & editing. **Pyuck-Pa Choi**: resources, data curation, writing – review & editing. **Subin Lee**: conceptualization, investigation, formal analysis, methodology, supervision, writing – review & editing. **Christoph Kirchlechner**: conceptulaization, supervision, funding acquisition, writing – review & editing.

Acknowledgments

U. B. acknowledges the financial support from Alexander von Humboldt Post-doctoral fellowship. TEM work was carried out with the support of the Karlsruhe Nano Micro Facility (KNMFi, www.knmf.kit.edu), a Helmholtz Research Infrastructure at Karlsruhe Institute of Technology (KIT, www.kit.edu).

Open Access funding enabled and organized by Projekt DEAL.

Funding

This study was supported by Alexander von Humboldt-Stiftung.

Conflicts of Interest

The authors declare no conflicts of interest.

Data Availability Statement

Data available on request from the authors.

References

1. R. C. Reed, *The Superalloys: Fundamentals and Applications*, 1st ed. (Cambridge University Press, 2006), https://doi.org/10.1017/CBO9780511541285.

2. R. Cozar and A. Pineau, "Morphology of y' and y" Precipitates and Thermal Stability of Inconel 718 type Alloys," *Metallurgical Transactions* 4 (1973): 47–59, https://doi.org/10.1007/BF02649604.

3. A. J. Detor, R. DiDomizio, R. Sharghi-Moshtaghin, et al., "Enabling Large Superalloy Parts Using Compact Coprecipitation of γ′ and γ″," *Metallurgical and Materials Transactions A* 49 (2018): 708–717, https://doi.org/10.1007/s11661-017-4356-7.

4. Y. Zhang, L. Lan, and Y. Zhao, "Effect of Precipitated Phases on the Mechanical Properties and Fracture Mechanisms of Inconel 718 Alloy," *Materials Science and Engineering: A* 864 (2023): 144598, https://doi.org/10.1016/j.msea.2023.144598.

5. F. R. Caliari, K. C. G. Candioto, A. A. Couto, C.Â. Nunes, and D. A. P. Reis, "Effect of Double Aging Heat Treatment on the Short-Term Creep Behavior of the Inconel 718," *Journal of Materials Engineering and Performance* 25 (2016): 2307–2317, https://doi.org/10.1007/s11665-016-2051-2.

6. F. Theska, A. Stanojevic, B. Oberwinkler, S. P. Ringer, and S. Primig, "On Conventional versus Direct Ageing of Alloy 718," *Acta Materialia* 156 (2018): 116–124, https://doi.org/10.1016/j.actamat.2018.06.034.

7. S. Mukhopadhyay, H. Sriram, C. H. Zenk, et al., "Creep Behavior of Compact γ′-γ″ Coprecipitation Strengthened IN718-Variant Superalloy," *Metals* 11 (2021): 1897, https://doi.org/10.3390/met11121897.

8. J. P. Collier, S. H. Wong, J. K. Tien, and J. C. Phillips, "The Effect of Varying AI, Ti,and Nb Content on the Phase Stability of INCONEL 718,"

Metallurgical Transactions A 19 (1988): 1657–1666, https://doi.org/10.1007/BF02645133.

9. J. He, G. Han, S. Fukuyama, and K. Yokogawa, "Interfaces in a Modified Inconel 718 with Compact Precipitates," *Acta Materialia* 46 (1998): 215–223, https://doi.org/10.1016/S1359-6454(97)00221-8.

10. Y. M. Eggeler, K. V. Vamsi, and T. M. Pollock, "Precipitate Shearing, Fault Energies, and Solute Segregation to Planar Faults in Ni-, CoNi-, and Co-Base Superalloys," *Annual Review of Materials Research* 51 (2021): 209–240, https://doi.org/10.1146/annurev-matsci-102419-011433.

11. J. M. Oblak, D. S. Duvall, and D. F. Paulonis, "An Estimate of the Strengthening Arising from Coherent, Tetragonally-Distorted Particles," *Materials Science and Engineering* 13 (1974): 51–56, https://doi.org/10.1016/0025-5416(74)90020-2.

12. M. Sundararaman, P. Mukhopadhyay, and S. Banerjee, "Deformation Behaviour of γ″ Strengthened Inconel 718," *Acta Metallurgica* 36 (1988): 847–864, https://doi.org/10.1016/0001-6160(88)90139-3.

13. C. H. Zenk, L. Feng, D. McAllister, Y. Wang, and M. J. Mills, "Shearing Mechanisms of Co-Precipitates in IN718," *Acta Materialia* 220 (2021): 117305, https://doi.org/10.1016/j.actamat.2021.117305.

14. M. Sundararaman and P. Mukhopadhyay, "Thermal Stability of Deformation Twins in γ′-Strengthened Alloy 718," *Defect and Diffusion Forum* 213 (2003): 61–74, https://doi.org/10.4028/www.scientific.net/DDF.213-215.61.

15. D. McAllister, "Shearing Mechanisms and Complex Particle Growth in Nickel Superalloy 718," (Doctoral dissertation, Ohio State University, 2016), http://rave.ohiolink.edu/etdc/view?acc_num=osu1461079188.

16. J. M. Oblak, D. F. Paulonis, and D. S. Duvall, "Coherency Strengthening in Ni Base Alloys Hardened by DO_{22} γ′ Precipitates," *Metallurgical Transactions* 5 (1974): 143–153, https://doi.org/10.1007/BF02642938.

17. D. C. Lv, D. McAllister, M. J. Mills, et al., "Deformation Mechanisms of $D0_{22}$ Ordered Intermetallic Phase in Superalloys," *Acta Materialia* 118 (2016): 350–361, https://doi.org/10.1016/j.actamat.2016.07.055.

18. P. M. Mignanelli, N. G. Jones, E. J. Pickering, et al., "Gamma-Gamma Prime-Gamma Double Prime Dual-Superlattice Superalloys," *Scripta Materialia* 136 (2017): 136–140, https://doi.org/10.1016/j.scriptamat.2017.04.029.

19. P. M. Mignanelli, N. G. Jones, M. C. Hardy, and H. J. Stone, "The Influence of Al: Nb Ratio on the Microstructure and Mechanical Response of Quaternary Ni–Cr–Al–Nb Alloys," *Materials Science and Engineering: A* 612 (2014): 179–186, https://doi.org/10.1016/j.msea.2014.06.021.

20. J. A. Manriquez, P. L. Bretz, L. Radenberg, and J. K. Tien, "The High Temperature Stability of IN718 Derivative Alloys," in Superalloys 1992 (Seventh International Symposium), (TMS, 1992), 507–516, https://doi.org/10.7449/1992/Superalloys_1992_507_516.

21. P. M. Mignanelli, N. G. Jones, M. C. Hardy, and H. J. Stone, "On the Time-Temperature-Transformation Behavior of a New Dual-Superlattice Nickel-Based Superalloy," *Metallurgical and Materials Transactions A* 49 (2018): 699–707, https://doi.org/10.1007/s11661-017-4355-8.

22. N. Zhou, D. C. Lv, H. L. Zhang, et al., "Computer Simulation of Phase Transformation and Plastic Deformation in IN718 Superalloy: Microstructural Evolution during Precipitation," *Acta Materialia* 65 (2014): 270–286, https://doi.org/10.1016/j.actamat.2013.10.069.

23. B. B. Dash, S. Dixit, C. J. Boehlert, M. Sundararaman, and S. Sankaran, "Influence of Interrupted Ageing on the Temporal Evolution of the γ′ Size Distribution and the Co-Precipitation of γ″ in Alloy 718Plus," *Materials Characterization* 206 (2023): 113394, https://doi.org/10.1016/j.matchar.2023.113394.

24. C. Rodenkirchen, A. K. Ackerman, P. M. Mignanelli, et al., "Effect of Alloying on the Microstructure, Phase Stability, Hardness, and Partitioning Behavior of a New Dual-Superlattice Nickel-Based Superalloy," *Metallurgical and Materials Transactions A* 54 (2023): 1902–1923, https://doi.org/10.1007/s11661-023-06972-7.

25. P. Beardmore and R. G. Davies, O n the Temperature Dependence of the Flow Stress of Nickel-Base Alloys, n.d.

26. E. Nembach, J. Pesicka, and E. Langmaack, "The High-Temperature Decrease of the Yield Strength of the γ′-Strengthened Superalloys NIMONIC PE16 and NIMONIC. 105," *Materials Science and Engineering: A* 362 (2003): 264–273, https://doi.org/10.1016/S0921-5093(03)00593-8.

27. N. Karpstein, M. Lenz, A. Bezold, M. Wu, S. Neumeier, and E. Spiecker, "Reliable Identification of the Complex or Superlattice Nature of Intrinsic and Extrinsic Stacking Faults in the L12 Phase by High-Resolution Imaging," *Acta Materialia* 260 (2023): 119284, https://doi.org/10.1016/j.actamat.2023.119284.

28. P. J. Phillips, D. McAllister, Y. Gao, et al., "Nano γ′/γ″ Composite Precipitates in Alloy 718," *Applied Physics Letters* 100 (2012): 211913, https://doi.org/10.1063/1.4721456.

29. H. Zhang, Y. Li, T. Ma, et al., "Tailoring of Nanoscale γ′ Precipitates and Unveiling Their Strengthening Mechanisms in Multimodal Nickel-Based Superalloy GH4720Li," *Materials Characterization* 188 (2022): 111918, https://doi.org/10.1016/j.matchar.2022.111918.

30. G. Kumari, M. Sundararaman, C. J. Boehlert, et al., "Strengthening Mechanisms for Microstructures Containing Unimodal and Bimodal γ′ Precipitates in ATI. 718Plus," *Materials Science and Engineering: A.* 908 (2024): 146928, https://doi.org/10.1016/j.msea.2024.146928.

31. K. Sun, P. Huang, and F. Wang, "The Bimodal Nanocoherent Precipitates Leads to Superior Strength-Ductility Synergy in a Novel CoCrNi-Based Medium Entropy Alloy," *Journal of Alloys and Compounds* 909 (2022): 164809, https://doi.org/10.1016/j.jallcom.2022.164809.

32. X. Zhang and T. Chen, "Bimodal Microstructure Dispersed with Nanosized Precipitates Makes Strong Aluminum Alloy with Large Ductility," *Materials & Design* 191 (2020): 108695, https://doi.org/10.1016/j.matdes.2020.108695.

33. U. Bansal, M. P. Singh, S. Mondol, et al., "The Interplay of Precipitation of Ordered Compounds and Interfacial Segregation in Al-Cu-Hf-Si Alloys for High-Temperature Strength," *Acta Materialia* 240 (2022): 118355, https://doi.org/10.1016/j.actamat.2022.118355.

34. U. Bansal, M. P. Singh, S. K. Sinha, et al., "Strength and Stability through Variable Micro Segregation Behaviour of Ta and Zr Solutes at Intermetallic Interfaces in Al-Cu Alloys," *Acta Materialia* 259 (2023): 119254, https://doi.org/10.1016/j.actamat.2023.119254.

35. X. Wei, L. Jin, F. Wang, et al., "High Strength and Ductility Mg-8Gd-3Y-0.5Zr Alloy with Bimodal Structure and Nano-Precipitates," *Journal of Materials Science & Technology* 44 (2020): 19–23, https://doi.org/10.1016/j.jmst.2019.10.024.

36. J. Zhang, Q. Na, T. Ma, et al., "Multimodal γ′ Phase Precipitation and Mechanical Properties of Co-Based Superalloys with Ta Addition," *Materials Science and Engineering: A* 932 (2025): 148250, https://doi.org/10.1016/j.msea.2025.148250.

37. J. Zhang, Q. Na, F. Lu, et al., "Insights into the Multimodal γ′ Precipitation in Co-Based Superalloys," *Materials Science and Engineering: A* 917 (2024): 147389, https://doi.org/10.1016/j.msea.2024.147389.

38. E. I. Galindo-Nava, L. D. Connor, and C. M. F. Rae, "On the Prediction of the Yield Stress of Unimodal and Multimodal γ ′ Nickel-Base Superalloys," *Acta Materialia* 98 (2015): 377–390, https://doi.org/10.1016/j.actamat.2015.07.048.

39. Q. He, F. Pan, F. Guo, et al., "Synergistic Strengthening by Bimodal Co-Precipitates: Strengthen Mechanisms in a New Directly Aged Corrosion-Resistance Nickel-Based Alloy," *Journal of Materials Research and Technology* 36 (2025): 9840–9850, https://doi.org/10.1016/j.jmrt.2025.05.167.

40. A. W. Zhu, A. Csontos, and E. A. Starke, "Computer Experiment on Superposition of Strengthening Effects of Different Particles," *Acta*

Materialia 47 (1999): 1713–1721, https://doi.org/10.1016/S1359-6454(99)00077-4.

41. S. Wang, L. Li, G. Chen, et al., "Modeling the Effect of Precipitation Spatial Geometry and Size Distribution on the Yield Strength of Aluminum Alloys," *Acta Mechanica* 234 (2023): 4323–4342, https://doi.org/10.1007/s00707-023-03608-0.

42. X. Deng, "Precipitation Strengthening of Stress-Aged Al-Cu-Mg-Ag Alloy Single Crystals," *Materials Science and Engineering: A* 819 (2021): 141458, https://doi.org/10.1016/j.msea.2021.141458.

43. A. Liu, F. Zhao, W. Huang, et al., "Effect of Aging Temperature on Precipitates Evolution and Mechanical Properties of GH4169 Superalloy," *Crystals* 13 (2023): 964, https://doi.org/10.3390/cryst13060964.

Supporting Information

Additional supporting information can be found online in the Supporting Information section.